

Article

# Modelling of the Superplastic Deformation of the Near- $\alpha$ Titanium Alloy (Ti-2.5Al-1.8Mn) Using Arrhenius-Type Constitutive Model and Artificial Neural Network

Ahmed Mosleh <sup>1,2</sup> , Anastasia Mikhaylovskaya <sup>1</sup>, Anton Kotov <sup>1,\*</sup>, Theo Pourcelot <sup>1,3</sup>, Sergey Aksenov <sup>4</sup>, James Kwame <sup>5</sup> and Vladimir Portnoy <sup>1</sup>

<sup>1</sup> Department of Physical Metallurgy of Non-Ferrous Metals, National University of Science and Technology “MISIS”, Leninsky Prospekt, 4, 119049 Moscow, Russia; mosleh@misis.ru (A.Mo.); mihaylovskaya@misis.ru (A.Mi.); theo.pourcelot7@gmail.com (T.P.); portnoy@misis.ru (V.P.)

<sup>2</sup> Shoubra Faculty of Engineering, Benha University, Shoubra St. 108, Shoubra, P.O. 11629, Cairo 11629, Egypt

<sup>3</sup> European School of Engineers and Materials Science of Nancy (EEIGM), University of Lorraine, 54000 Nancy, France

<sup>4</sup> Moscow Institute of Electronics and Mathematics, National Research University Higher School of Economics, Tallinskaya 34, 123458 Moscow, Russia; aksenov.s.a@gmail.com

<sup>5</sup> Advanced Forming Research Centre, University of Strathclyde, 85 Inchinnan Dr, Inchinnan, Renfrew PA4 9LJ, UK; james.kwame@strath.ac.uk

\* Correspondence: kotov@misis.ru; Tel.: +7-909-646-9480

Received: 10 November 2017; Accepted: 11 December 2017; Published: 15 December 2017

**Abstract:** The paper focuses on developing constitutive models for superplastic deformation behaviour of near- $\alpha$  titanium alloy (Ti-2.5Al-1.8Mn) at elevated temperatures in a range from 840 to 890 °C and in a strain rate range from  $2 \times 10^{-4}$  to  $8 \times 10^{-4} \text{ s}^{-1}$ . Stress–strain experimental tensile tests data were used to develop the mathematical models. Both, hyperbolic sine Arrhenius-type constitutive model and artificial neural-network model were constructed. A comparative study on the competence of the developed models to predict the superplastic deformation behaviour of this alloy was made. The fitting results suggest that the artificial neural-network model has higher accuracy and is more efficient in fitting the superplastic deformation flow behaviour of near- $\alpha$  Titanium alloy (Ti-2.5Al-1.8Mn) at superplastic forming than the Arrhenius-type constitutive model. However, the tested results revealed that the error for the artificial neural-network is higher than the case of Arrhenius-type constitutive model for predicting the unmodelled conditions.

**Keywords:** superplasticity; titanium alloys; constitutive modelling; arrhenius-type constitutive equation; artificial neural network; activation energy

## 1. Introduction

The flow behaviour of material during hot forming process is usually complicated. The hardening and softening mechanisms both mainly affect the strain rate and temperature [1–3]. The understanding of metallic alloys deformation behaviour at elevated temperatures helps to provide information about the metal forming processes. Three main categories of models are utilised to describe the stress flow behavior of metallic alloys: (1) physical based; (2) phenomenological and (3) artificial neural network constitutive models [4–8]. Phenomenological constitutive models are usually used in the simulation of hot forming processes due to their practicability and accuracy. For titanium alloys, the more significant part of literature on the constitutive modelling pays particular attention to  $\alpha + \beta$  type alloys, especially Ti-6Al-4V titanium alloy [8–11]. The Arrhenius-type constitutive equation (ACE), where the flow

stress is expressed by the hyperbolic laws, was first proposed by Jonas et al. [12]. Many studies have used the Arrhenius hyperbolic equation to establish the flow stress of different metallic alloys during deformation at elevated temperatures [6,7].

Recently, artificial neural network (ANN) has provided fundamentally novel and different approaches for materials modelling and processing control from statistical or numerical methods [13]. ANN architecture consists of an input layer, an output layer and one or several hidden layers. Those parts are connected to form a unit called neurons. The input layer is set up to collect data from outside. The output layer sends back the information to the users. The number of hidden layers can vary in function from the amount of data put in the input and output layer. In fact, the hidden layer has the ability of simplifying the complexity of a non-linear problem. The main idea of ANN analysis is to minimise the differences between the known targets of the inputs and the ANN outputs. Therefore, ANN has the capabilities to adjust, memorise and anticipate. Thus, it is thought to be more efficient than regression equations thanks to its extrapolation and interpolation of specific data ranges capabilities. This method provides a new way of using examples of a precise function to find the model constants that will make a specific mapping function with the aim of approximating the function as precisely as possible [14,15]. Furthermore, ANN is especially more suitable in the treatment of non-linear and complicated relationships. It has been increasingly used for modelling the hot deformation behaviour of metallic materials [16,17]. ANN is capable of self and also recognises patterns in a series of input and output values without any prior natural assumptions. ANN does not require any physical knowledge about restoration criteria and deformation. Thus, it is readily suitable to model the hot deformation behaviour of materials in different treatment regimes. ANN offers a good option for modelling because it can keep the data in memory. It can deal with discrete data and adjust the old network to approximate the new experimental data [18]. ANN adjusts itself with the aim of reproducing the function target according to the training sample input. Due to their high ability of parallelism, ANN is truly suitable for estimating the flow stress from experimental data. A back-propagation neural network model was developed to predict the flow stress of Ti-6Al-4V  $\alpha + \beta$  type alloy [19]. The authors of [19] highlighted the possibility of the successful training of the ANN in both  $\beta$  and  $\alpha + \beta$  phase regions. The Arrhenius-type model and the artificial neural network were developed for other Ti40 stable  $\beta$  type titanium alloy [16] and a good agreement between the predicted and the experimental flow stress values was observed in the case of the ANN model.

The purpose of the current study was to suggest a suitable approach for modelling and predicting the deformation behaviour of near- $\alpha$  Ti-2.5Al-1.8Mn alloy, based on superplastic tensile tests data. The Arrhenius constitutive equations were applied to describe the relationship between the flow stress, deformation temperature and constant strain rate at superplastic conditions. The comprehensive model describes the compensation of the strain effect and proposes a relationship between the flow stress, strain rate and temperature of the alloys at elevated temperatures. An ANN model was also developed to predict the flow stress as a function of strain, strain rate and temperature. The validity of the detailed results based on the proposed ACE and ANN model were also compared. The correlation coefficient, the mean absolute relative error and the root mean square error were computed to evaluate the performance of both model types.

## 2. Materials and Experiments

Conventional sheets of Ti-2.5wt%Al-1.8wt%Mn alloy with a thickness of 1.55 mm were analysed. Superplastic indicators were determined using uniaxial tensile test on a Walter-Bay LFM100 test machine (Walter + Bai AG, Löhningen, Switzerland) with a DionPro program (Walter + Bai AG, Version. 4.80, Löhningen, Switzerland) service for the in-situ control traverse motion. The samples were cut parallel to the rolling direction by wire cutting electro-discharge machining process. The gage section size was 6 mm  $\times$  1.5 mm, and the gage length was 17 mm. Constant strain rate tests were performed in a temperature range of 840 to 890 °C and constant strain rate values of  $2 \times 10^{-4}$ ,  $6 \times 10^{-4}$  and  $8 \times 10^{-4}$  s<sup>-1</sup>.

The temperatures and strain rates were within the superplastic deformation strain rate–temperature range according to [20].

### 3. Test Results

Figure 1 shows the experimental flow stress curves obtained at a constant strain rate values of  $2 \times 10^{-4}$ ,  $4 \times 10^{-4}$  and  $8 \times 10^{-4} \text{ s}^{-1}$  and in a temperature range of 840 to 890 °C. It could be observed that the steady stage begun from the strain value of approximately 0.1. The flow stress values typically increase with increasing strain from 0.1 to 1.3 at all studied conditions. Temperature, strain rate and stress affected the strain hardening behaviour of the studied alloy due to dynamic grain growth phenomenon as described in [20].

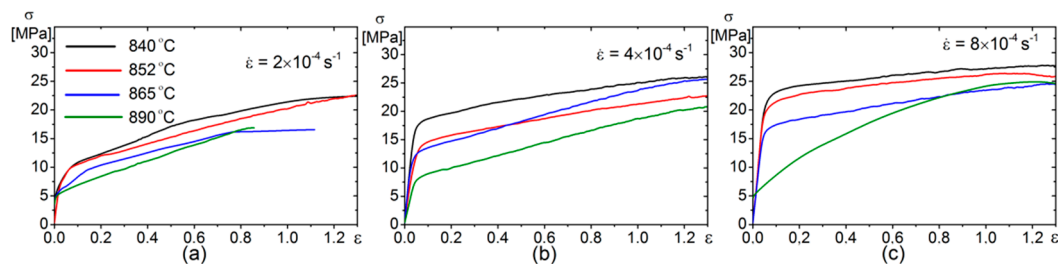


**Figure 1.** The true stress–strain curves of the tested alloy at various temperatures and various strain rates:  $2 \times 10^{-4} \text{ s}^{-1}$  (a),  $4 \times 10^{-4} \text{ s}^{-1}$  (b) and  $8 \times 10^{-4} \text{ s}^{-1}$  (c).

The stress–strain data obtained at the various test conditions were used to construct the ACE and ANN models to compare the predictability of both models.

### 4. Modeling Experiments

#### 4.1. Arrhenius Constitutive Model (ACE)

The influence of strain rate and temperature on deformation behaviour can be expressed via Zener–Holloman parameter ( $Z$ ) (Equation (1)) and an exponent-type equation (Equation (2)) [21–23].

$$Z = \dot{\epsilon} \exp\left(\frac{Q}{RT}\right) \quad (1)$$

$$\dot{\epsilon} = Af(\sigma)\exp\left(-\frac{Q}{RT}\right) \quad (2)$$

where  $A$  is a material constant,  $\dot{\epsilon}$  is a strain rate in  $\text{s}^{-1}$ ,  $T$  is a temperature in  $K$ , and  $Q$  is an effective activation energy of deformation in  $\text{kJ/mol}$ ,  $R$  is a gas constant =  $8.314 \text{ J}/(\text{mol}\cdot K)$ ,  $f(\sigma)$  is a function of flow stress, can be expressed as follows:

$$f(\sigma) = \begin{cases} \sigma^{n_1}, & \text{for } \alpha\sigma < 0.8 \\ \exp(\beta\sigma), & \text{for } \alpha\sigma > 1.2 \\ [\sinh(\alpha\sigma)]^{n_2}, & \text{for various } \sigma \end{cases} \quad (3)$$

where  $\beta$ ,  $n_1$ ,  $n_2$  and  $\alpha = \beta/n_1$  are the material constants. In general, Equation (3) is a power law function, which is appropriate for low stress level ( $\alpha\sigma < 0.8$ ). Equation (4) is an exponential law equation, which is used for high stress level ( $\alpha\sigma > 1.2$ ). Equation (5), a hyperbolic sine law, that typically applies to a wide stress range. Thus, the strain rate can be obtained by the following Equations:

$$\dot{\epsilon} = \begin{cases} A_1 \sigma^{n_1} \exp\left(-\frac{Q_1}{RT}\right) - \text{Power law} & (6) \\ A_2 e^{(\beta\sigma)} \exp\left(-\frac{Q_2}{RT}\right) - \text{Exponential law} & (7) \\ A_3 [\sinh(\alpha\sigma)]^{n_2} \exp\left(-\frac{Q_3}{RT}\right) - \text{Hyperbolic sine law} & (8) \end{cases}$$

4.1.1. Determination of the Arrhenius Constitutive Model Constants

The true stress and true strain data presented in Figure 1 was used to assess the material constants of the constitutive Equations (6)–(8). The true strain of 0.4 (50%) was used as an example to describe the typical procedures of the material constants determination. The following Equations (9) and (10) were obtained by taking the natural logarithm of both sides of Equations (6) and (7):

$$\ln \dot{\epsilon} = \ln A_1 + n_1 \ln \sigma - \frac{Q_1}{RT} \Rightarrow n_1 = \left[ \frac{\partial \ln \dot{\epsilon}}{\partial \ln \sigma} \right]_T \quad (9)$$

$$\ln \dot{\epsilon} = \ln A_2 + \beta \sigma - \frac{Q_2}{RT} \Rightarrow \beta = \left[ \frac{\partial \ln \dot{\epsilon}}{\partial \sigma} \right]_T \quad (10)$$

Figure 2 demonstrates the  $\ln \dot{\epsilon} - \ln \sigma$  (Figure 2a),  $\ln \dot{\epsilon} - \sigma$  (Figure 2b),  $\ln \dot{\epsilon} - \ln \sinh(\alpha\sigma)$  (Figure 2c) and  $\ln \sinh(\alpha\sigma) - \frac{1000}{RT}$  (Figure 2d) linear plots. The slope of plots in Figure 2 varies in limited range. The values of  $n_1$ ,  $\beta$  and  $Q_{1,2}$  were calculated as the mean values of the slopes of the  $\ln \dot{\epsilon} - \ln \sigma$  and  $\ln \dot{\epsilon} - \sigma$  plots, respectively (Figure 2a,b).

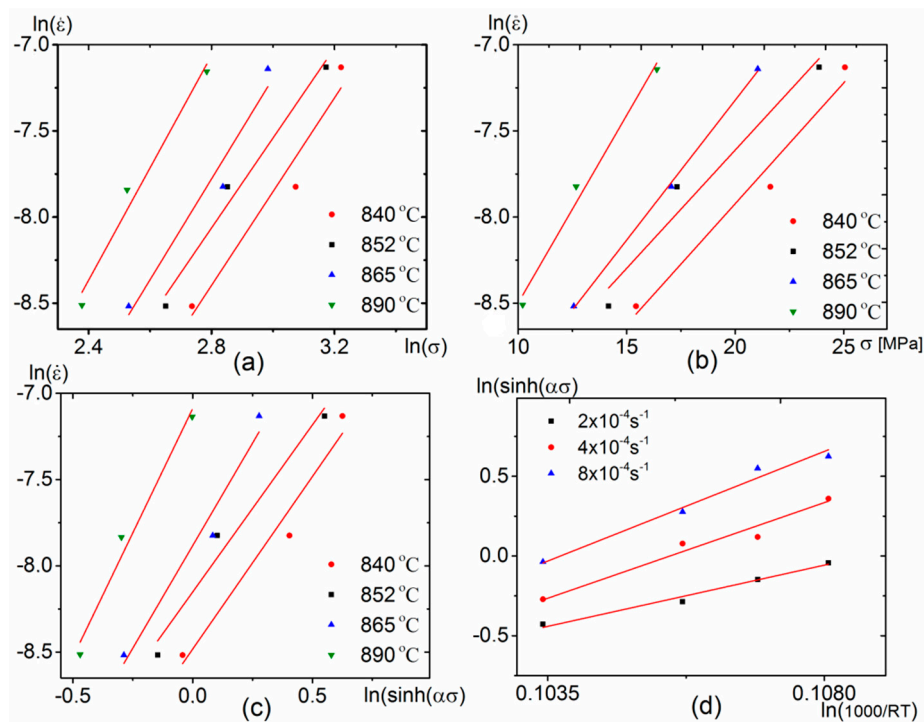


Figure 2. The plots of  $\ln \dot{\epsilon} - \ln \sigma$  (a);  $\ln \dot{\epsilon} - \sigma$  (b); plots of  $\ln \dot{\epsilon} - \ln \sinh(\alpha\sigma)$  (c); and  $\ln \sinh(\alpha\sigma) - \frac{1000}{RT}$  (d).

Equation (11) was obtained by taking the natural logarithm of both sides of Equation (8) to calculate the  $Q_3$  and  $n_2$  values:

$$\ln \dot{\epsilon} = \ln A_3 + n_2 \ln \sinh(\alpha\sigma) - \frac{Q_3}{RT} \quad (11)$$

Equations (12) and (13) were obtained by the partial differentiation of Equation (11):

$$n_2 = \left[ \frac{\partial \ln \dot{\epsilon}}{\partial \ln[\sinh(\alpha\sigma)]} \right]_T \quad (12)$$

$$Q_3 = R \times \left[ \frac{\partial \ln \dot{\epsilon}}{\partial \ln[\sinh(\alpha\sigma)]} \right]_T \times \left[ \frac{\partial \ln[\sinh(\alpha\sigma)]}{\partial \left(\frac{1}{T}\right)} \right]_{\dot{\epsilon}} \quad (13)$$

Thus, the  $n_2$  and  $Q_3$  values were achieved from the slope of  $\ln \dot{\epsilon} - \ln \sinh(\alpha\sigma)$  and  $\ln \sinh(\alpha\sigma) - \frac{1000}{RT}$  plotted lines, which are shown in Figure 2c,d.

$Q_1$  and  $Q_2$  calculated as same as  $Q_3$  as follows:

$$Q_1 = R \times \left[ \frac{\partial \ln \dot{\epsilon}}{\partial \ln \sigma} \right]_T \times \left[ \frac{\partial \ln \sigma}{\partial \left(\frac{1}{T}\right)} \right]_{\dot{\epsilon}} \quad (14)$$

$$Q_2 = R \times \left[ \frac{\partial \ln \dot{\epsilon}}{\partial \sigma} \right]_T \times \left[ \frac{\partial \sigma}{\partial \left(\frac{1}{T}\right)} \right]_{\dot{\epsilon}} \quad (15)$$

The model parameters at a strain of 0.4 (50%) are collected in Table 1.

**Table 1.** The calculated values of  $A_1$ ,  $A_2$ ,  $A_3$ ,  $n_1$ ,  $n_2$ ,  $\beta$ ,  $Q_{1,2,3}$  and  $\alpha$  constants of Arrhenius-type constitutive equation (ACE) model.

$\ln(A_1)$	$n_1/m^*$	$Q_1$ [KJ/mol]	$\ln(A_2)$	$\beta$ [MPa <sup>-1</sup> ]	$Q_2$ [KJ/mol]	$\alpha$	$\ln(A_3)$	$n_2$	$Q_3$ [KJ/mol]
14.6	2.8/0.35	287 ± 12	17.5	0.162	265 ± 10	0.057	21.5	2.166	279 ± 15

\* The strain rate sensitivity  $m$ -index values were determined as  $m = \frac{1}{n_1}$ .

The relationship between  $T$ ,  $\dot{\epsilon}$ , and  $\sigma$  can be expressed as follows:

$$\dot{\epsilon} = A_3 [\sinh(\alpha\sigma)]^{n_2} \exp\left(-\frac{Q_3}{RT}\right) \quad (16)$$

$$\dot{\epsilon} = 2.5 \times 10^9 [\sinh(0.057\sigma)]^{2.166} \exp\left(-\frac{279 \times 1000}{RT}\right) \quad (17)$$

Zener–Hollomon parameter  $Z$  can be used to describe the flow stress according to the hyperbolic sine law.

$$\sigma = \frac{1}{\alpha} \ln \left\{ \left( \frac{Z}{A_3} \right)^{\frac{1}{n_2}} + \left[ \left( \frac{Z}{A_3} \right)^{\frac{2}{n_2}} + 1 \right]^{\frac{1}{2}} \right\} \quad (18)$$

where  $Z = \dot{\epsilon} \exp\left(\frac{Q_3}{RT}\right)$  (Equation (1)).

Finally, the flow stress ( $\sigma$ ) versus and the strain rate ( $\dot{\epsilon}$ ) can be described by the follow equation:

$$\sigma = \frac{1}{0.057} \ln \left\{ \left( \frac{\dot{\epsilon} \exp\left(\frac{279 \times 10^3}{RT}\right)}{2.5 \times 10^9} \right)^{\frac{1}{2.166}} + \left[ \left( \frac{\dot{\epsilon} \exp\left(\frac{279 \times 10^3}{RT}\right)}{2.5 \times 10^9} \right)^{\frac{2}{2.166}} + 1 \right]^{\frac{1}{2}} \right\} \quad (19)$$

#### 4.1.2. Compensation of Strain Effect

It is known that strain affects the material constants [24,25]. Thus, the strain effect on the material constants should be considered in order to predict the flow stress behavior at deformation. The material

constants were determined at different strains within the strain range of 0.1–1.1, as shown in Figure 3. It was considered that the material constants ( $\alpha$ ,  $n_2$ ,  $Q_3$  and  $\ln(A_3)$ ) exhibit a polynomial relation with the strains according to [24–26].

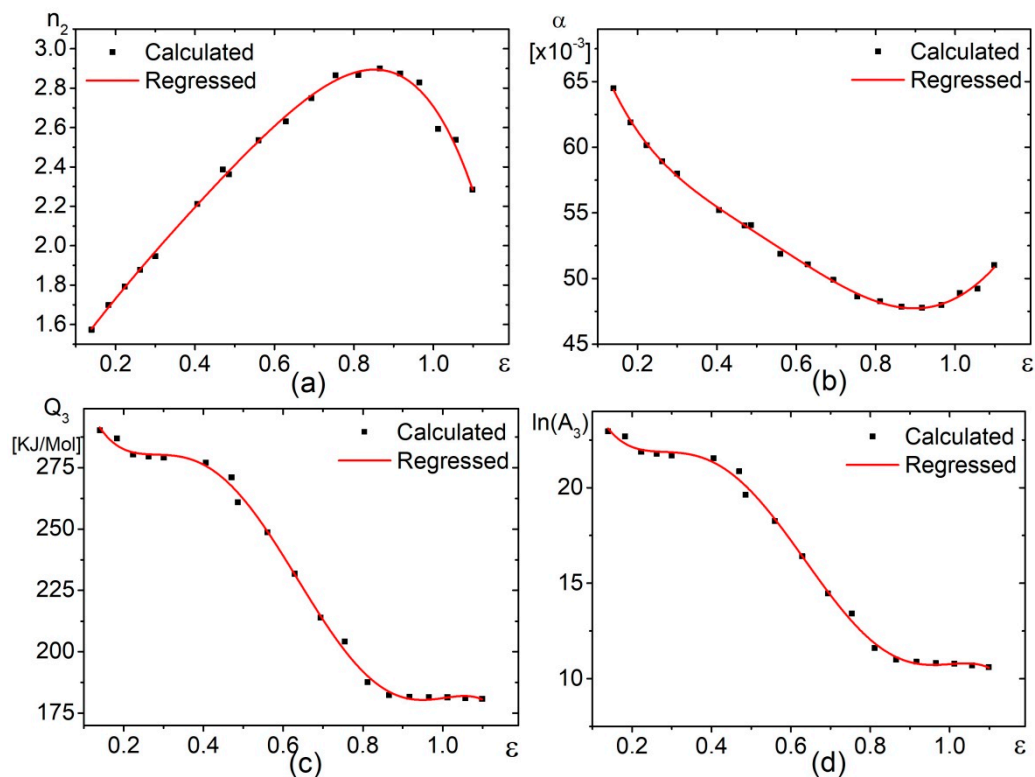


**Figure 3.** The dependence of  $n_2$  (a),  $\alpha$  (b),  $Q_3$  (c) and  $\ln(A_3)$  (d) constants vs true strain ( $\epsilon$ ).

The stress exponent  $n_2$  is typically used to identify the dominant mechanism that controlled the hot deformation process. Thus, the different superplastic deformation mechanisms can be associated with various  $n_2$  values. According to [27,28], grain boundary sliding and dislocation viscous glide mechanism may lead to  $n$  values close to 2 and 3 respectively and the mechanisms related to  $n$  values in the range of 4 to 6 are associated with dislocation climb. The relationship between  $n_2$  and the strain is consistent with the downward parabola. As shown in Figure 3a, most  $n_2$  values vary from 1.6 to 2.9. Current  $n_2$  values and previously published results of the grain and dislocation structure analysis [20] permits the prediction of the deformation mechanisms and their evolution with increasing strain. The symbioses between the dislocation viscous glide and the grain boundary sliding mechanisms can be used to suggest the deformation controlled mechanism due to  $n_2$  evolution. The grain structure at the start of deformation was partially unrecrystallised. Grain boundary sliding is the main deformation mechanism in the recrystallised volume at the beginning of deformation; thus, the  $n_2$  is closer to 2. The results showed an increase in the value of  $n_2$  to 3 with increasing strain up to 0.8. Grain boundary sliding occurs simultaneously with continuous dynamic recrystallisation in the deformed and the substructured volume with increasing strain. The decrease in the  $n_2$  value at larger strains may be due to the formation of recrystallized grain structure in all tested specimen and the active grain boundary sliding is accommodated by dislocation mechanisms. High dislocation activity in the  $\alpha$ -phase was observed at superplastic deformation of the studied alloy at both small strain of 0.7 and large strain of 1.6. Moreover, a fraction of the deformed  $\beta$ -phase is increased with increasing strain according to [20], which suggested that significant deformation of the  $\beta$ -phase occurred due to the dislocation mechanisms.

The material constant  $\alpha$  (Figure 3b) presents an overall downward trend with the increase of strain up to 0.8. Constant  $\alpha$  decreases in a strain range of 0.8 to 1.0 and insignificantly change in a strain range of 1.0 to 1.1.

The effective activation energy of deformation also suggested the specific deformation mechanisms and the accompanying processes [29]. The effective activation energy ( $Q_3$ ) versus strain (Figure 3c) and  $\ln(A_3)$  versus strain (Figure 3d) curves exhibit similar behaviour. The effective activation energy  $Q_3$  varies in a range from 285 to 180 kJ/mol for the different strain values in a studied temperature range (Figure 3c). The  $Q_3$  decreased significantly to a strain value of 0.8 and insignificantly changed. The decrease in  $Q_3$  with increasing strain is in agreement with [25,27,28,30]. The decreasing  $Q_3$  value clearly indicates a decrease in the amount of stored energy in the material due to deformation [24,29]. Dislocation density at low strains can decrease due to dynamic recovery and recrystallisation at the beginning of the superplastic deformation, which occurred at low strains in the studied alloy according to [20]. The decrease in crystal defects leads to the formation of more equilibrium states and lower  $Q_3$ .

The activation energies of the grain boundary self-diffusion are 183 kJ·mol<sup>-1</sup> in  $\alpha$ -Ti and 153 kJ/mol<sup>-1</sup> in  $\beta$ -Ti [31]. The intergranular diffusion activation energy is significantly higher for both phases (from 200 to 360 kJ·mol<sup>-1</sup> [31]). The constitutive model predicts the effective activation energy of approximately 180 kJ·mol<sup>-1</sup> at strains above 0.7. This value is close to the activation energy for the grain boundary self-diffusion in  $\alpha$ -Ti. Therefore, the effective activation energy value can be associated with the grain boundary sliding mechanism [32], which is in agreement with the superplastic phenomenon description [33].

Based on the value of  $R^2$ , the fifth order polynomial was found to represent it more accurately. The material parameters  $\alpha$ ,  $n_2$  and  $\ln(A_3)$  have good correlation coefficient Equation (20) which means that their behavior can be modeled using the polynomial equations. The coefficients of the polynomial function are presented in Table 2.

$$\begin{cases} \alpha = Y_{10} + B_{11}\varepsilon^1 + B_{12}\varepsilon^2 + B_{13}\varepsilon^3 + B_{14}\varepsilon^4 + B_{15}\varepsilon^5 \\ n_2 = Y_{20} + B_{21}\varepsilon^1 + B_{22}\varepsilon^2 + B_{23}\varepsilon^3 + B_{24}\varepsilon^4 + B_{25}\varepsilon^5 \\ A_3 = Y_{30} + B_{31}\varepsilon^1 + B_{32}\varepsilon^2 + B_{33}\varepsilon^3 + B_{34}\varepsilon^4 + B_{35}\varepsilon^5 \\ Q_3 = Y_{40} + B_{41}\varepsilon^1 + B_{42}\varepsilon^2 + B_{43}\varepsilon^3 + B_{44}\varepsilon^4 + B_{45}\varepsilon^5 \end{cases} \quad (20)$$

**Table 2.** The coefficient of the polynomial for  $\alpha$ ,  $n_2$ ,  $A_3$  and  $Q_3$  and the  $R^2$  for this coefficient.

Parameter	$Y_0$	$B_1$	$B_2$	$B_3$	$B_4$	$B_5$	$R^2$
$\alpha$	$Y_{10} = 0.077$	$B_{11} = -0.135$	$B_{12} = 0.363$	$B_{13} = -0.55$	$B_{14} = 0.387$	$B_{15} = -0.096$	0.998
$n_2$	$Y_{20} = 1.19$	$B_{21} = 2.99$	$B_{22} = -1.57$	$B_{23} = 0.48$	$B_{24} = 2.193$	$B_{25} = -2.58$	0.995
$\ln(A_3)$	$Y_{30} = 33.17$	$B_{31} = -137.03$	$B_{32} = 621.85$	$B_{33} = -1272$	$B_{34} = 1112.9$	$B_{35} = -348.2$	0.997
$Q$	$Y_{40} = 384.76$	$B_{41} = -1269.25$	$B_{42} = 5751.1$	$B_{43} = -11,719$	$B_{44} = 10,220.4$	$B_{45} = -3187$	0.997

After determining the material constants, the flow stress at an effective strain rate was predicted using Equation (16).

#### 4.1.3. Verification of the Arrhenius Constitutive Equations Model

In order to evaluate the accuracy of the developed ACE equations, a comparison between the fitted and the experimented stress values was performed. The performance of the developed model is evaluated by calculating the correlation coefficient ( $R$ ) (Equation (21)), average absolute relative error (AARE) (Equation (22)) and the root mean square error (RMSE) (Equation (23)):

$$R = \frac{\sum_{i=1}^N (E_i - \bar{E})(P_i - \bar{P})}{\sqrt{\sum_{i=1}^N (E_i - \bar{E})^2 \sum_{i=1}^N (P_i - \bar{P})^2}} \quad (21)$$

$$AARE = \frac{1}{N} \sum_{i=1}^N \left| \frac{E_i - P_i}{E_i} \right| \quad (22)$$

$$RMSE = \sqrt{\frac{1}{N} \sum_{i=1}^N (E_i - P_i)^2} \quad (23)$$

where  $E_i$  is the experimental flow stress, and  $P_i$  is the fitted flow stress obtained from the modified constitutive equation.  $\bar{E}$  and  $\bar{P}$  are the mean values of the experimental and the fitted flow stress values, respectively.  $N$  is the total data number that used in current research.  $R$  is the statistical index which is typically used to reflect the quality of the correlation between different coefficients. To be useful, the correlation coefficient  $R$  requires a significant amount of data. For instance, if the  $N$  is too small, the method that provides a relationship between the experimental and the predicted stress may be identified due to the  $R$ . In addition, the average absolute relative error (AARE) is an unbiased statistical parameter which may indicate the predictability of an equation and can be calculated term by term.

Figure 4 shows the experimental stress–strain curves with verification of the constitutive equations and the correlation between them in a temperature range of 840–890 °C and a strain rate range of  $2 \times 10^{-4}$ – $8 \times 10^{-4} \text{ s}^{-1}$ . It is found that the predicted stresses have a good agreement with the experimental stresses. The values of  $R$ , AARE and RMSE are 97.25%, 3.4% and 1.09, respectively. Thus, the results reflect a reasonable predictability of the modified constitutive equation (Figure 4d).

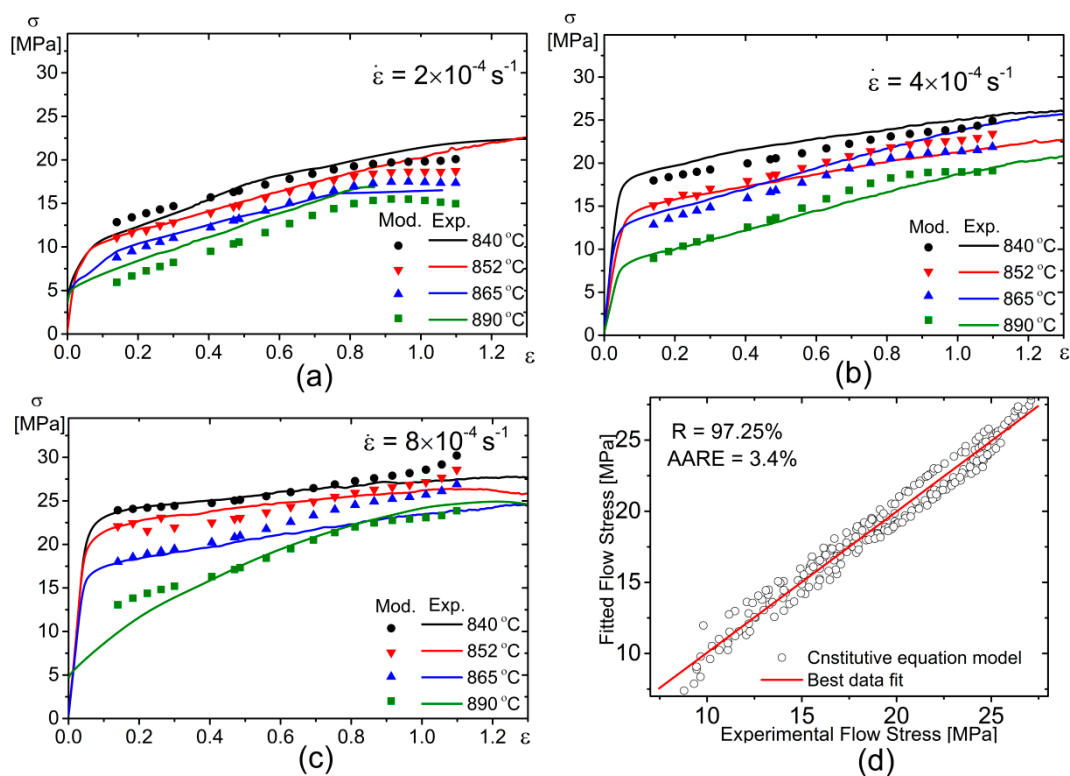


**Figure 4.** The true stress–strain curves of the tested alloy at different temperatures and different strain rates with verification of the constitutive equation (through points): (a)  $2 \times 10^{-4} \text{ s}^{-1}$ ; (b)  $4 \times 10^{-4} \text{ s}^{-1}$ ; (c)  $8 \times 10^{-4} \text{ s}^{-1}$  and (d) the correlation between experimental and fitted flow stress.

#### 4.2. Artificial Neural Network Analysis

A typical ANN model is generally constructed using various steps, such as: (i) collecting the data; (ii) determining the input/output (target) parameters; (iii) analysing and pre-processing the experimental data; (iv) training the ANN; (v) testing the trained ANN; and, finally, (vi) evaluating



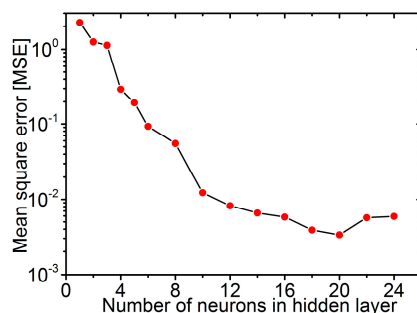


**Figure 6.** Dependence of the mean Square error versus number of neurons in the hidden layer.

The network's predictions are refined to approximate the experimental data during training on the basis of the availability of data and the reliability of the target. Training functions, transfer function and training algorithm should be chosen for ANN. In this investigation, the transfer functions that have been used are tan-sigmoid and purelin. The trained network should be tested to show an appropriate reliability and accuracy. Among various possible learning algorithms, the back-propagation algorithm is the most popular utilised for training the ANN [40]. ANN with BP algorithm learns by adjusting the weights, and these adjustments are stored as knowledge.

In this work, the most suitable network was developed to predict the superplastic deformation behaviour of near- $\alpha$  Titanium alloy Ti-2.5Al-1.8Mn alloy. The optimised ANN model consists of three input neurones; a single hidden layer with 20 neurones, one output neurone with transfer functions of 'tan-sigmoid' and 'pure linear'. The feed forward BP algorithm is used to train the ANN. The ANN training parameters are presented in Table 3. The work was carried out by using the neural network toolbox available in MATLAB 2015b software. The goal of MSE for the training was set as  $10^{-6}$ . One complete pass through a set of input–output pairs during the training of the network was considered as an epoch [34]. The network was trained to stabilise the error values that was reached after approximately 8000 epochs. It is in agreement with [34].

**Table 3.** Settings of training parameters for the neural network.

Name of Network Parameters	Contents
Network	Back-Propagation
Training function	TrainLM
Performance function	MSE
Training epoch	8000
Goal	$1 \times 10^{-6}$
Transfer function of hidden layer	Tan-sigmoid
Transfer function of output	Liner (purelin)

Figure 7 shows the comparison and the correlation between the fitted and the experimental stresses obtained from the ANN model. As shown, the fitted stresses have an excellent agreement with the experimental stresses at all values of temperature and strain rate. The values of the performance indicators  $R$ , AARE and RMSE are 99.98 %, 0.33 % and 0.079 respectively. These values are more accurate than the constitutive equations model. It is in agreement with results observed in other studies [34–44].

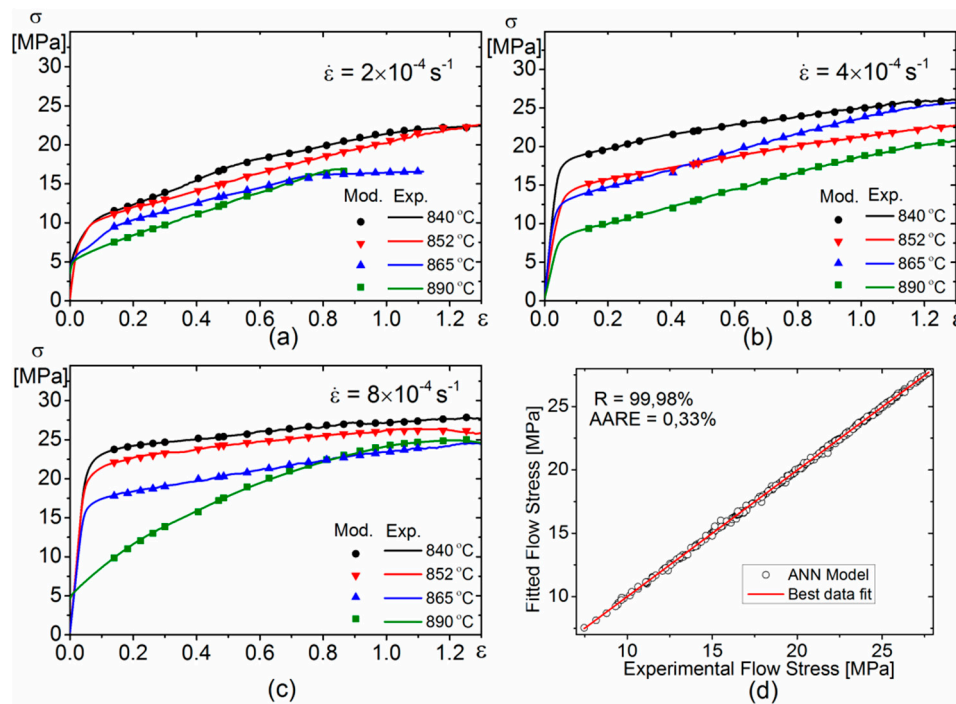


**Figure 7.** The true stress–strain curves of the tested alloy at different temperatures and different strain rates with verification of artificial neural network (ANN): (a)  $2 \times 10^{-4} \text{ s}^{-1}$ ; (b)  $4 \times 10^{-4} \text{ s}^{-1}$ ; (c)  $8 \times 10^{-4} \text{ s}^{-1}$  and (d) correlation between experimental and predicted flow stress.

### 5. Cross-Validation of the Models

In order to find which of the two models (ACE or ANN) predicts the material behaviour better, the cross-validation procedure was utilized. Both models were verified by extracting the stress–strain experimental curves one by one and twelve trial datasets were constructed as listed in Table 4. Both models were subsequently reconstructed for each trial dataset and the predictions made for conditions of excluded stress–strain curve were compared with the experimental data.

**Table 4.** The excluded conditions in trial datasets.

Trial Number	Excluded Conditions	
	Temperature (°C)	Strain Rate ( $\text{s}^{-1}$ )
Trial-1	840	$2 \times 10^{-4}$
Trial-2	840	$4 \times 10^{-4}$
Trial-3	840	$8 \times 10^{-4}$
Trial-4	852	$2 \times 10^{-4}$
Trial-5	852	$4 \times 10^{-4}$
Trial-6	852	$8 \times 10^{-4}$
Trial-7	865	$2 \times 10^{-4}$
Trial-8	865	$4 \times 10^{-4}$
Trial-9	865	$8 \times 10^{-4}$
Trial-10	890	$2 \times 10^{-4}$
Trial-11	890	$4 \times 10^{-4}$
Trial-12	890	$8 \times 10^{-4}$

Figure 8 shows the material constants versus strain curves calculated for each trial dataset. The material constants nearly exhibit the same behaviour with increasing strain for all trials except for Trails 1 and 12. When the curve at 890 °C and  $8 \times 10^{-4} \text{ s}^{-1}$  was excluded (Trial 12), the effective

activation energy at lower strains exhibits lower values compared to the other trials. Conversely, the effective activation energy is higher at lower strains compared to other trials in the case of 840 °C and  $2 \times 10^{-4} \text{ s}^{-1}$  (Trial 1). Trail 1 and Trail 12 are data extremes (Trail 1 is minimum temperature and minimum strain rate; Trail 12 is maximum temperature and maximum strain rate). The extreme points exhibited different behavior compared with the other trails because, the temperature and strain rate were narrow, resulting in simulation error. Simulation error of extremes points can be decreased by increasing the temperature and strain rate ranges. Unfortunately, this observation is cumbersome to analyze because the current alloy exhibits superplasticity in limited temperature–strain rate ranges which were studied.

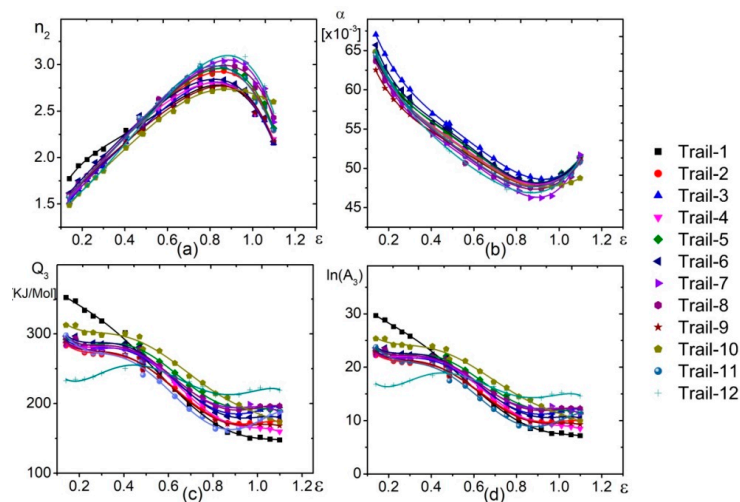


**Figure 8.** Variation of  $n_2$ ,  $\alpha$ ,  $Q_3$  and  $\ln(A_3)$  with true strain for all trails:  $n_2$  (a);  $\alpha$  (b);  $Q_3$  (c); and  $\ln(A_3)$  (d) using Arrhenius-type constitutive equation (ACE) model.

The error between the experimental and predicted flow stress was calculated as follows (Equation (25)):

$$Error = \frac{1}{\epsilon_{max}} \int_0^{\epsilon_{max}} |\sigma_{exp}(\epsilon) - \sigma_{mod}(\epsilon)| d\epsilon \tag{25}$$

where  $\sigma_{exp}(\epsilon)$  and  $\sigma_{mod}(\epsilon)$  are the experimental and the predicted flow stresses given as functions of effective strain ( $\epsilon$ ) respectively,  $\epsilon_{max}$  is the value of the maximum strain. Figure 9 shows the comparison of the stress–strain curves constructed for Trial-3 (Figure 9a) and the errors between the experimental flow stress and the predicted flow stress of both models (Figure 9b).

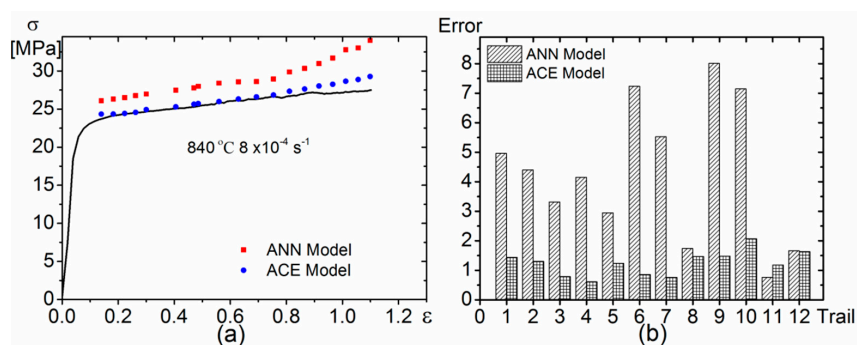


**Figure 9.** Comparison between the experimental flow stress and Predicted flow stress from both models (a) and the Error between experimental and tested flow stress (b).

It can be clearly seen that even though the ANN model was more accurate in the approximation and the fitting of the initial data than ACE, the ANN error for all trials is higher than that of ACE error (Figure 9). However, after both models have been tested by cross-validation technique, the ACE model exhibits better predictability of the stress values at superplastic deformation compared to the ANN model.

## 6. Conclusions

Hot tension tests were performed to characterise the flow behaviour of near- $\alpha$  titanium alloy Ti-2.5Al-1.8Mn in a temperature range of 840–890 °C, a strain rate range of  $2 \times 10^{-4}$ – $8 \times 10^{-4}$  s<sup>-1</sup> and a true strain range of 0.1–1.1. The Arrhenius-type constitutive equation (ACE) and the Artificial Neural Network (ANN) were developed to model the superplastic deformation behaviour of the studied alloy.

The following conclusions were drawn from the current results:

- (1) The values of  $\alpha$ ,  $n_2$ ,  $Q_3$  and  $A_3$  in the Arrhenius-type hyperbolic constitutive equation were found to be the function of strain in the studied strain rate–temperature–strain range. The material constant versus strain dependence suggested that, the symbiosis between the dislocation viscous glide and the grain boundary sliding are the deformation mechanisms.
- (2) The correlation coefficient ( $R$ ), the mean absolute relative error (AARE) and the root mean square error (RMSE) obtained from the developed ACE and ANN are 95.25%, 5.2% and 1.09, respectively for the constitutive equations. In the case of ANN, the value of  $R$ , AARE and RMSE are 99.97%, 0.32% and 0.079 respectively. The ANN model exhibits higher accuracy and much better efficiency in approximating the hot deformation behaviour than the ACE at the points used for training in ANN.
- (3) Both models were verified by extracting the stress–strain experimental curves one by one, and comparing their predictability following the cross-validation approach. The ACE model exhibits better predictability of the superplastic deformation behavior as compared to the ANN model. An important outcome of this analysis is that, despite the rising popularity of the artificial neural networks, one should exercise caution when using them for predicting mechanical behaviour of materials. Cross-validation should be mandatory for such kind of ANN usage. In some cases, as shown in this work, the verification technique demonstrated that the classical approach based on the constitutive equations of Arrhenius type is more effective and reliable than the artificial neural networks.

**Acknowledgments:** The work was partially funded by the state task for universities Russian Federation (#11.7172.2017/8.9). Anton Kotov acknowledges the President Grant No. MK-2301.2017.8. The contribution of Sergey Aksenov is supported in the framework of the Basic Research Program at the National Research University Higher School of Economics (HSE).

**Author Contributions:** Ahmed Mosleh and Theo Pourcelot designed and performed the constitutive models and analysed the data; Ahmed Mosleh and Anastasia Mikhaylovskaya conceived and design the experiments, and wrote the paper. Anton Kotov and James Kwame designed and performed the tensile test experiments; Sergey Aksenov designed and discussed the results of the models verification; Vladimir Portnoy analysed and discussed the results and supervised the experiments.

**Conflicts of Interest:** The authors declare no conflict of interest. The founding sponsors had no role in the design of the study; in the collection, analyses, or interpretation of data; in the writing of the manuscript, and in the decision to publish the results.

## References

1. Franciosi, P.; Berbenni, S. Heterogeneous crystal and poly-crystal plasticity modeling from a transformation field analysis within a regularized Schmid law. *J. Mech. Phys. Solids* **2007**, *55*, 2265–2299. [[CrossRef](#)]
2. Sommitsch, C.; Sievert, R.; Wlanis, T.; Günther, B.; Wieser, V. Modelling of creep-fatigue in containers during aluminium and copper extrusion. *Comput. Mater. Sci.* **2007**, *39*, 55–64. [[CrossRef](#)]

3. Dan, W.J.; Zhang, W.G.; Li, S.H.; Lin, Z.Q. A model for strain-induced martensitic transformation of TRIP steel with strain rate. *Comput. Mater. Sci.* **2007**, *40*, 101–107. [[CrossRef](#)]
4. Haghdadadi, N.; Zarei-Hanzaki, A.; Abedi, H.R. The flow behavior modeling of cast A356 aluminum alloy at elevated temperatures considering the effect of strain. *Mater. Sci. Eng. A* **2012**, *535*, 252–257. [[CrossRef](#)]
5. Marandi, A.; Zarei-Hanzaki, A.; Haghdadadi, N.; Eskandari, M. The prediction of hot deformation behavior in Fe-21Mn-2.5Si-1.5Al transformation-twinning induced plasticity steel. *Mater. Sci. Eng. A* **2012**, *554*, 72–78. [[CrossRef](#)]
6. Zhang, H.; Wen, W.; Cui, H.; Xu, Y. A modified Zerilli-Armstrong model for alloy IC10 over a wide range of temperatures and strain rates. *Mater. Sci. Eng. A* **2009**, *527*, 328–333. [[CrossRef](#)]
7. Voyiadjis, G.Z.; Almasri, A.H. A physically based constitutive model for fcc metals with applications to dynamic hardness. *Mech. Mater.* **2008**, *40*, 549–563. [[CrossRef](#)]
8. Lin, Y.C.; Chen, X.-M. A critical review of experimental results and constitutive descriptions for metals and alloys in hot working. *Mater. Des.* **2011**, *32*, 1733–1759. [[CrossRef](#)]
9. Vanderhastan, M.; Rabet, L.; Verlinden, B. Ti-6Al-4V: Deformation map and modelisation of tensile behavior. *Mater. Des.* **2008**, *29*, 1090–1098. [[CrossRef](#)]
10. Cai, J.; Li, F.; Liu, T.; Chen, B.; He, M. Constitutive equations for elevated temperature flow stress of Ti-6Al-4V alloy considering the effect of strain. *Mater. Des.* **2011**, *32*, 1144–1151. [[CrossRef](#)]
11. Shafaat, M.A.; Omidvar, H.; Fallah, B. Prediction of hot compression flow curves of Ti-6Al-4V alloy in  $\alpha+\beta$  phase region. *Mater. Des.* **2011**, *32*, 4689–4695. [[CrossRef](#)]
12. Jonas, J.J.; Sellars, C.M.; Tegart, W.J.M. Strength and structure under hot-working conditions. *Metall. Rev.* **1969**, *14*, 1–24. [[CrossRef](#)]
13. Bahrami, A.; Anijdan, S.H.M.; Hosseini, H.R.M.; Shafyei, A.; Narimani, R. Effective parameters modeling in compression of an austenitic stainless steel using artificial neural network. *Comput. Mater. Sci.* **2005**, *34*, 335–341. [[CrossRef](#)]
14. Guo, Z.; Malinov, S.; Sha, W. Modelling beta transus temperature of titanium alloys using artificial neural network. *Comput. Mater. Sci.* **2005**, *32*, 1–12. [[CrossRef](#)]
15. Malinov, S.; Sha, W. Application of artificial neural networks for modelling correlations in titanium alloys. *Mater. Sci. Eng. A* **2004**, *365*, 202–211. [[CrossRef](#)]
16. Sun, Y.; Zeng, W.D.; Zhao, Y.Q.; Zhang, X.M.; Shu, Y.; Zhou, Y.G. Modeling constitutive relationship of Ti40 alloy using artificial neural network. *Mater. Des.* **2011**, *32*, 1537–1541. [[CrossRef](#)]
17. Mandal, S.; Sivaprasad, P.V.; Venugopal, S. Capability of a Feed-Forward Artificial Neural Network to Predict the Constitutive Flow Behavior of As Cast 304 Stainless Steel Under Hot Deformation. *J. Eng. Mater. Technol.* **2006**, *129*, 242–247. [[CrossRef](#)]
18. Qin, Y.J.; Pan, Q.L.; He, Y.B.; Li, W.B.; Liu, X.Y.; Fan, X. Artificial Neural Network Modeling to Evaluate and Predict the Deformation Behavior of ZK60 Magnesium Alloy During Hot Compression. *Mater. Manuf. Process.* **2010**, *25*, 539–545. [[CrossRef](#)]
19. Reddy, N.S.; Lee, Y.H.; Park, C.H.; Lee, C.S. Prediction of flow stress in Ti-6Al-4V alloy with an equiaxed  $\alpha+\beta$  microstructure by artificial neural networks. *Mater. Sci. Eng. A* **2008**, *492*, 276–282. [[CrossRef](#)]
20. Mikhaylovskaya, A.V.; Mosleh, A.O.; Kotov, A.D.; Kwame, J.S.; Pourcelot, T.; Golovin, I.S.; Portnoy, V.K. Superplastic deformation behaviour and microstructure evolution of near- $\alpha$  Ti-Al-Mn alloy. *Mater. Sci. Eng. A* **2017**, *708*, 469–477. [[CrossRef](#)]
21. Samantaray, D.; Mandal, S.; Bhaduri, A.K.; Sivaprasad, P.V. An overview on constitutive modelling to predict elevated temperature flow behaviour of fast reactor structural materials. *Trans. Indian Inst. Met.* **2010**, *63*, 823–831. [[CrossRef](#)]
22. Zener, C.; Hollomon, J.H. Effect of Strain Rate Upon Plastic Flow of Steel. *J. Appl. Phys.* **1944**, *15*, 22–32. [[CrossRef](#)]
23. Sellars, C.M.; McTegart, W.J. On the mechanism of hot deformation. *Acta Metall.* **1966**, *14*, 1136–1138. [[CrossRef](#)]
24. Rao, K.P.; Hawbolt, E.B. Development of Constitutive Relationships Using Compression Testing of a Medium Carbon Steel. *J. Eng. Mater. Technol.* **1992**, *114*, 116–123. [[CrossRef](#)]
25. Mandal, S.; Rakesh, V.; Sivaprasad, P.V.; Venugopal, S.; Kasiviswanathan, K.V. Constitutive equations to predict high temperature flow stress in a Ti-modified austenitic stainless steel. *Mater. Sci. Eng. A* **2009**, *500*, 114–121. [[CrossRef](#)]

26. Lin, Y.C.; Chen, M.-S.; Zhong, J. Constitutive modeling for elevated temperature flow behavior of 42CrMo steel. *Comput. Mater. Sci.* **2008**, *42*, 470–477. [[CrossRef](#)]
27. Mahmudi, R.; Rezaee-Bazzaz, A.; Banaie-Fard, H.R. Investigation of stress exponent in the room-temperature creep of Sn-40Pb-2.5Sb solder alloy. *J. Alloys Compd.* **2007**, *429*, 192–197. [[CrossRef](#)]
28. Langdon, T.G. Identifying creep mechanisms at low stresses. *Mater. Sci. Eng. A* **2000**, *283*, 266–273. [[CrossRef](#)]
29. Yang, X.; Guo, H.; Liang, H.; Yao, Z.; Yuan, S. Flow Behavior and Constitutive Equation of Ti-6.5Al-2Sn-4Zr-4Mo-1W-0.2Si Titanium Alloy. *J. Mater. Eng. Perform.* **2016**, *25*, 1347–1359. [[CrossRef](#)]
30. Pu, Z.J.; Wu, K.H.; Shi, J.; Zou, D. Development of constitutive relationships for the hot deformation of boron microalloying TiAlCrV alloys. *Mater. Sci. Eng. A* **1995**, *192–193*, 780–787. [[CrossRef](#)]
31. Weiss, I.; Semiatin, S.L. Thermomechanical processing of alpha titanium alloys—An overview. *Mater. Sci. Eng. A* **1999**, *263*, 243–256. [[CrossRef](#)]
32. Frost, H.J.; Ashby, M.F. *Deformation Mechanism Maps: The Plasticity and Creep of Metals and Ceramics*, 1st ed.; Pergamon Press: New York, NY, USA, 1982; p. 166. ISBN 0080293379.
33. Nieh, T.G.; Wadsworth, J.; Sherby, O.D. *Superplasticity in Metals and Ceramics*, 1st ed.; Cambridge University Press: Cambridge, UK, 1997; p. 288. ISBN 100521561051.
34. Zhao, J.; Ding, H.; Zhao, W.; Huang, M.; Wei, D.; Jiang, Z. Modelling of the hot deformation behaviour of a titanium alloy using constitutive equations and artificial neural network. *Comput. Mater. Sci.* **2014**, *92*, 47–56. [[CrossRef](#)]
35. Genel, K.; Kurnaz, S.C.; Durman, M. Modeling of tribological properties of alumina fiber reinforced zinc–aluminum composites using artificial neural network. *Mater. Sci. Eng. A* **2003**, *363*, 203–210. [[CrossRef](#)]
36. Hornik, K.; Stinchcombe, M.; White, H. Multilayer feedforward networks are universal approximators. *Neural Netw.* **1989**, *2*, 359–366. [[CrossRef](#)]
37. Wu, S.W.; Zhou, X.G.; Cao, G.M.; Liu, Z.Y.; Wang, G.D. The improvement on constitutive modeling of Nb-Ti micro alloyed steel by using intelligent algorithms. *Mater. Des.* **2017**, *116*, 676–685. [[CrossRef](#)]
38. Guo, L.F.; Li, B.C.; Xue, Y.; Zhang, Z.M. Constitutive Relationship Model of Al-W Alloy Using Artificial Neural Network. *Adv. Mater. Res.* **2014**, *1004–1005*, 1120–1124. [[CrossRef](#)]
39. Ji, G.; Li, F.; Li, Q.; Li, H.; Li, Z. A comparative study on Arrhenius-type constitutive model and artificial neural network model to predict high-temperature deformation behaviour in Aermet100 steel. *Mater. Sci. Eng. A* **2011**, *528*, 4774–4782. [[CrossRef](#)]
40. Sun, Y.; Zeng, W.D.; Zhao, Y.Q.; Qi, Y.L.; Ma, X.; Han, Y.F. Development of constitutive relationship model of Ti600 alloy using artificial neural network. *Comput. Mater. Sci.* **2010**, *48*, 686–691. [[CrossRef](#)]
41. Peng, W.; Zeng, W.; Wang, Q.; Yu, H. Comparative study on constitutive relationship of as-cast Ti60 titanium alloy during hot deformation based on Arrhenius-type and artificial neural network models. *Mater. Des.* **2013**, *51*, 95–104. [[CrossRef](#)]
42. Li, H.Y.; Wei, D.D.; Li, Y.H.; Wang, X.F. Application of artificial neural network and constitutive equations to describe the hot compressive behavior of 28CrMnMoV steel. *Mater. Des.* **2012**, *35*, 557–562. [[CrossRef](#)]
43. Haghdadi, N.; Zarei-Hanzaki, A.; Khalesian, A.R.; Abedi, H.R. Artificial neural network modeling to predict the hot deformation behavior of an A356 aluminum alloy. *Mater. Des.* **2013**, *49*, 386–391. [[CrossRef](#)]
44. Guo, L.; Li, B.; Zhang, Z. Constitutive relationship model of TC21 alloy based on artificial neural network. *Trans. Nonferr. Met. Soc. China* **2013**, *23*, 1761–1765. [[CrossRef](#)]

